



# Methane activation and oxidation over $\text{La}_{0.8}\text{Sr}_{0.2}\text{Ga}_{0.8}\text{Mg}_{0.2}\text{O}_{3-\alpha}$ : H/D exchange study

Dmitriy M. Zakharov \* 

Institute of High-Temperature Electrochemistry , Ekaterinburg 620137, Russia

\* Corresponding author: [d.zakharov@ihte.ru](mailto:d.zakharov@ihte.ru)



## Abstract

The mechanism of methane activation and oxidation over  $\text{La}_{0.8}\text{Sr}_{0.2}\text{Ga}_{0.8}\text{Mg}_{0.2}\text{O}_{3-\alpha}$  (LSGM) has been investigated using hydrogen isotope exchange with gas phase equilibration. The measurements have been conducted in a temperature range of 300–700 °C in pure methane and in a mixture of methane and hydrogen under  $p\text{CH}_4$  of 100, 200, and 500 Pa and  $p\text{H}_2$  of 200 Pa. LSGM has been shown to exhibit catalytic activity to C–H bond splitting in methane in the temperature range of 550–700 °C. The mechanism of methane activation comprises two parallel reaction pathways, with the first pathway related to  $\text{CH}_3$  and H species formation and the second pathway related to stepwise methane dissociation to carbon atoms. The ability of LSGM to consume hydrogen from methane is determined. The formation of carbon deposit and CO on LSGM decomposition was observed at temperature  $\geq 750$  °C.

## Key findings

- Methane activation mechanism for LSGM involves two parallel exchange pathways
- Hydrogen incorporation into LSGM structure is the rate-determining step of the activation mechanism.
- LSGM exhibit phase stability in dry methane atmosphere up to 750 °C.

© 2025, the Authors. This article is published in open access under the terms and conditions of the Creative Commons Attribution (CC BY) license (<http://creativecommons.org/licenses/by/4.0/>).

## Accompanying information

### Article history

Received: 15.10.25

Revised: 01.11.25

Accepted: 02.11.25

Available online: 07.11.25


### Keywords

LSGM; lanthanum gallate; H/D exchange; methane; hydrogen; isotope exchange

### Funding

The research was supported by the Russian Science Foundation and the Government of Sverdlovsk oblast (project number 24-23-20001), <https://rscf.ru/en/project/24-23-20001/>.

### Supplementary information

Transparent peer review: 

### Sustainable Development Goals



## 1. Introduction

Solid oxides remain of considerable interest owing to their potential applications in heterogeneous catalysis and renewable energy production [1, 2], particularly in electrochemical devices such as solid oxide and proton ceramic electrochemical devices (SOEDs and PCEDs), including fuel cells [2, 3], electrolysis cells [4–6], reversible cells [7], and membrane reactors [8–11]. These devices utilize oxides exhibiting oxygen-ion, protonic or electronic conductivity to convert the energy of redox reactions between an oxidizer (e.g., air) and fuel gases (e.g.,  $\text{H}_2$ ,  $\text{H}_2\text{O}$ ,  $\text{CH}_4$ ) into electricity or purified gases, including hydrocarbons [1–11]. However, the devices commercialization is hindered by stringent requirements for materials with high chemical and thermal stability, compatibility, conductivity, and catalytic activity under oxidative and reductive conditions.

$\text{A(II)B(IV)O}_3$  and  $\text{A(III)B(III)O}_3$  perovskites of various compositions remain the primary oxide materials for SOEDs and PCEDs [12–19]. Among them, Sr- and Mg-doped

$\text{LaGaO}_3$  ( $\text{La}_{1-x}\text{Sr}_x\text{Ga}_{1-y}\text{Mg}_y\text{O}_{3-\alpha}$ ) is regarded as one of the most promising oxygen-conducting electrolytes in SOEDs [20–34] due to its high oxide-ion conductivity and thermal compatibility with other oxides.

Studies of hydrogen mass transfer, although fewer in number, suggest the possibility of protonic conductivity in  $\text{H}_2/\text{H}_2\text{O}$  atmospheres. On the one hand, some investigations [35–37] confirmed the protonic conductivity in  $\text{La}_{1-x}(\text{Sr},\text{Ba})_x\text{Ga}_{1-y}\text{Mg}_y\text{O}_{3-\alpha}$  via measurements of total conductivity, electromotive force, and hydrogen permeation. On the other hand, the authors of [28] reported its absence in  $\text{La}_{0.9}\text{Sr}_{0.1}\text{GaO}_{3-\alpha}$  under humid air. Recent H/D exchange studies between  $\text{H}_2$  and  $\text{a}_{0.8}\text{Sr}_{0.2}\text{Ga}_{0.8-y}\text{Mg}_{0.2}\text{Fe}_y\text{O}_{3-\alpha}$  reveal the oxide's catalytic activity toward H–H bond splitting [38, 39]. The mechanism involves dissociative  $\text{H}_2$  adsorption forming adsorbed hydrogen atoms, followed by their incorporation into the oxide lattice, influenced by charge transfer. In Fe-free oxides, hydrogen uptake is purely exothermic, as in other proton-conducting oxides [18, 19], whereas Fe-doped

variants exhibit mixed exothermic-endothermic regimes depending on the Fe cation oxidation states.

The interaction of light hydrocarbons, such as methane, with  $\text{La}_{1-x}\text{Sr}_x\text{Ga}_{1-y}\text{Mg}_y\text{O}_{3-\alpha}$  is less studied. Most works focus on the efficiency of SOEDs for methane partial oxidation using these oxides as membranes [40–44]. For instance, undoped and 3d-metal-doped  $\text{La}_{1-x}\text{Sr}_x\text{Ga}_{1-x-z}\text{Mg}_y\text{M}_z\text{O}_{3-\alpha}$  systems show higher power densities than YSZ, CSZ, or SDC electrolytes in methane partial oxidation to syngas at 1273 K with comparable conversion ratios [40, 41]. Doping with 3d metals enhances oxidative methane coupling performance, increasing power densities and conversion [41]. In the case of  $\text{La}_{0.7}\text{Sr}_{0.3}\text{Ga}_{0.6}\text{Fe}_{0.4}\text{O}_{3-\alpha}$  membranes the rate-determining step of methane partial oxidation is shown to be bulk oxygen diffusion in the oxide [42]. These findings are consistent with those of studies on amperometric methane sensors, where the sensitivity of the sensors correlates with oxygen-ion conductivity [43]. However, the side process of carbon deposition over Ni-doped  $\text{La}_{0.8}\text{Sr}_{0.2}\text{Ga}_{0.8}\text{Mg}_{0.2}\text{O}_{3-\alpha}$  during ethane/ethylene production under low  $\text{O}_2/\text{CH}_4$  ratios is reported in [44]. The process reduces the selectivity of the oxide over time.

Overall, research into Sr- and Mg-doped  $\text{LaGaO}_3$  remains focused on their role as oxygen-conducting membranes, with limited insights into methane interaction mechanisms. Attempts have been made to elucidate the roles of oxides in light hydrocarbon activation [45, 46]. Study [45] associates the catalytic activity of the oxides, along with their selectivity to ethane/ethylene and  $\text{CO}_2/\text{CO}$ , with varying oxygen anion binding energies. The authors of [45] propose a multistep mechanism, involving methane dissociation to methyl radicals (which recombine to form  $\text{C}_2$  hydrocarbons), oxidation to CO (catalyzed by strongly bound lattice oxygen), and CO to  $\text{CO}_2$  (catalyzed by adsorbed oxygen). These findings are consistent with those of a previous study [46]. However, both papers draw on reaction schemes for methane oxidative coupling developed for other oxide systems [47–49], while information on elementary steps and intermediates remains insufficient, with methyl radicals as the only proven intermediate [50]. Thus, this study aims to investigate the kinetics of methane activation over  $\text{La}_{0.8}\text{Sr}_{0.2}\text{Ga}_{0.8}\text{Mg}_{0.2}\text{O}_{3-\alpha}$  (LSGM) oxide, examining the effects of temperature, gas pressure, and hydrogen addition on reaction rates.

## 2. Materials and Methods

The as-synthesized  $\text{La}_{0.8}\text{Sr}_{0.2}\text{Ga}_{0.8}\text{Mg}_{0.2}\text{O}_{3-\alpha}$  (LSGM) powder was obtained from the previous study, in which the details of the synthesis and characterization of the oxide are presented [38]. The powder sample had a cubic structure with  $Pm\bar{3}m$  sp. gr. and <1.0 wt.% of impurities  $\text{La}_4\text{Ga}_2\text{O}_9$  and  $\text{SrLaFa}_3\text{O}_7$ , as determined by whole-powder-pattern fitting [38]. The elemental composition of the oxide was  $\text{La}_{0.78}\text{Sr}_{0.22}\text{Ga}_{0.82}\text{Mg}_{0.18}\text{O}_{2.80}$ . The specific surface area of the powder was  $1.07 \pm 0.01 \text{ m}^2/\text{g}$ .

The phase stability of the oxide in a methane atmosphere was analyzed by XRPD using a D/MAX-2200 diffractometer (Rigaku, Japan) with  $\text{Cu K}\alpha$  radiation ( $\lambda(\text{K}\alpha) = 1.5406 \text{ \AA}$ , 40kV, 30mA) at room temperature in ambient air. The measurements were carried out in the  $10\text{--}90^\circ$  range of  $2\theta$  with the step of  $0.02^\circ$ .

The processes of carbon deposition on LSGM were investigated with Raman spectroscopy using a Renishaw U 1000 microscope-spectrometer (Renishaw, United Kingdom) equipped with a 15 mW, 532 nm solid-state laser (LCM-S-111, Renishaw). The spectra were recorded over the wavenumber range  $50\text{--}2000 \text{ cm}^{-1}$  under a spectral resolution of  $1\text{--}2 \text{ cm}^{-1}$ . The laser beam spot size was  $1 \mu\text{m}$  and an exposure time was 30 s.

The kinetics of methane activation over LSGM was studied using hydrogen isotope exchange with gas phase equilibration (IE GPE). The experiments were conducted in the temperature range of  $300\text{--}800^\circ\text{C}$  under  $p\text{CH}_4$  of 100, 200, and 500 Pa and under a mixture of 100 Pa  $\text{CH}_4$  and 200 Pa of  $\text{H}_2$ . All experiments were conducted using the unique scientific setup “Isotope Exchange” described in [19, 38, 51]. At the beginning of the experiments, the surface of the LSGM powder was cleaned by heating under high vacuum ( $10^{-4} \text{ Pa}$ ) up to  $700^\circ\text{C}$  at a heating rate of  $60^\circ\text{C h}^{-1}$ ; next, the sample was exposed to 200 Pa of  $\text{H}_2$  (99.999 vol.% purity, natural isotope composition) for 1 h and cooled to  $300^\circ\text{C}$  at the same rate under 200 Pa of  $\text{H}_2$ . The experiments were conducted according to [51, 52], with pre-equilibration of the oxide under the required pressure of  $\text{CH}_4$  (99.999 vol.% purity, natural isotope composition) or a mixture of  $\text{CH}_4$  and  $\text{H}_2$ . The pre-equilibrated sample was then subjected to H/D exchange with  $\text{CD}_4$  (99.8 wt.% methane, 99.9 at.% D enrichment) or a mixture of  $\text{H}_2$  and  $\text{CD}_4$  at the same partial pressures as the gas in the reactor chamber with the sample to maintain chemical equilibrium / stationary conditions. Between the experiments, the sample was maintained under 200 Pa of  $\text{H}_2$  to prevent any oxidation of the sample surface in accordance with [38]. The gas-phase isotope composition was analyzed *in situ* using a quadrupole mass spectrometer (Microvision 2 Vision 2000P, MKS Instruments, USA). The mole fractions of the gas phase components were calculated using a two-layered artificial neural network, as discussed in [51].

## 3. Isotope exchange theory

The model of the five types of exchange was used to describe the kinetics of H/D exchange between methane and LSGM [17, 51–53]. The model considers isotope exchange between any molecule with four exchangeable hydrogen atoms and the hydrogen of a solid as purely statistical. In this case, all possible activation mechanisms in the system can be expressed through the five types of exchange [53]. Each type of exchange indicates the number of hydrogen atoms exchanged between the molecules in the gas phase and the solid during an elementary act of exchange. The five types

of exchange can be expressed in terms of the set of linear atom transfer reactions (1)–(5):



In reactions (1)–(5) A is a random hydrogen isotope D or H,  $A_4$  is a methane isotopologue with an arbitrary isotope composition ( $\text{CH}_4$ ,  $\text{CH}_3\text{D}$ ,  $\text{CH}_2\text{D}_2$ ,  $\text{CHD}_3$ , and  $\text{CD}_4$ ),  $A_S$  is random hydrogen isotope in the solid, and  $A_M$  represents random hydrogen isotope in methane; the values  $r_0$ ,  $r_1$ ,  $r_2$ ,  $r_3$  and  $r_4$  denote the rates of the respective atom transfer reactions. The system of differential equations and isotope variables describing isotope exchange according to the model is discussed in detail in [51] and is not presented here for brevity.

It was shown [17, 51, 53] that the main kinetic parameters describing the catalytic activity of the solid in the given system are the total rate of exchange ( $r$ ) calculated by equation (6) and the rate of hydrogen surface exchange ( $r_H$ ). The former represents the sum rate of methane dissociative adsorption across all parallel dissociative adsorption steps per unit surface per unit time. The latter represents the average number of hydrogen atoms exchanged between the two phases per unit surface and time.

$$r = \sum_{k=0}^4 r_k, \quad (6)$$

$$r_H = \frac{1}{4} \sum_{k=0}^4 k r_k, \quad (7)$$

where  $k$  is the index number of the respective exchange type, indicating the number of hydrogen atoms transferred between a methane molecule and the solid by this type.

The H/D exchange in the three-component system of  $\text{CH}_4$ ,  $\text{H}_2$ , and LSGM was described based on a three-component model of one-atom exchange in accordance with [54]. The model considers the change in isotope enrichment in the exchange components ( $\delta$ ) during the exchange process. Formally, the exchange according to the model can be presented by three linear one-atom transfer reactions (8)–(10):



where  $A_H$  is a random atom in  $\text{H}_2$  of arbitrary isotope composition,  $r_{H2}$  is the rate of hydrogen heteromolecular exchange

between methane and  $\text{H}_2$  through the solid surface, and  $r_{H3}$  is the rate of hydrogen surface exchange between  $\text{H}_2$  and the solid, having the same meaning as  $r_H$ . The differential equation system for the model is presented elsewhere [54].

Since reactions (1)–(5) and (8)–(10) are linear, the general kinetic equations describing isotope exchange by these models can be presented in vector form as follows:

$$v_A = e^{R\tau} v_A(0), \quad (11)$$

where  $R$  is the square matrix containing the rates of atom transfer reactions for the models,  $v_A$  and  $v_A(0)$  are the column vectors containing isotope variables for the models at time  $\tau$  and zero-time, respectively. The variables can be presented by the mole fractions of  $A_4$ ,  $A_S$ ,  $A_H$ , and  $A_M$ , the products of the mole fractions of  $A_S$ ,  $A_H$ , and  $A_M$ , or the other variables, as discussed in [51, 54].

## 4. Results and Discussion

### 4.1. Kinetics of H/D exchange between methane and LSGM

The time dependences of methane isotopologue mole fractions in methane and deuterium enrichment of methane ( $\delta_M = \frac{1}{4} \sum_{i=0}^4 i x_i$ , where  $i$  is the number of D atoms in the molecule) obtained from H/D exchange between  $\text{CH}_4$  and LSGM in the temperature range 500–700 °C at  $p\text{CH}_4 = 100$  Pa are presented in Figure 1. The figure shows that the exchange activity of LSGM to C–H dissociation starts at temperatures higher than 500 °C and gradually increases with temperature. A slight decrease in  $\delta_M$  with time is observed in the temperature range 600–700 °C, suggesting the consumption of D from methane by LSGM bulk.

Figure 1 shows the model curves obtained from the results of fitting the data with the model of five exchange types with black lines. The curves closely match the experimental data, suggesting an acceptable agreement between the model and the obtained data.

Figure 2a presents the Arrhenius plot of the total rate of exchange ( $r$ ) and the rate of hydrogen surface exchange ( $r_H$ ) between methane and LSGM in comparison with the rates obtained in [38] for 200 Pa of pure  $\text{H}_2$  atmosphere obtained in [38]. The figure shows that in the whole studied temperature range  $r_H$  values are more than 1 order of magnitude lower than that of  $r$  which suggest the methane adsorption-related steps to be generally faster than that of incorporation. The comparison of the rates with those obtained in pure  $\text{H}_2$  atmosphere indicates that the catalytic activity of LSGM to  $\text{H}_2$  activation is significantly higher than that to methane activation. Nevertheless, in both cases  $r_H$  values are lower than  $r$ , which indirectly confirms that one of the types of adsorbed species in the methane atmosphere is hydrogen adatoms, suggesting that the methane activation mechanism includes methane dissociative adsorption and the incorporation of hydrogen adsorbed atoms as one of the activation steps.

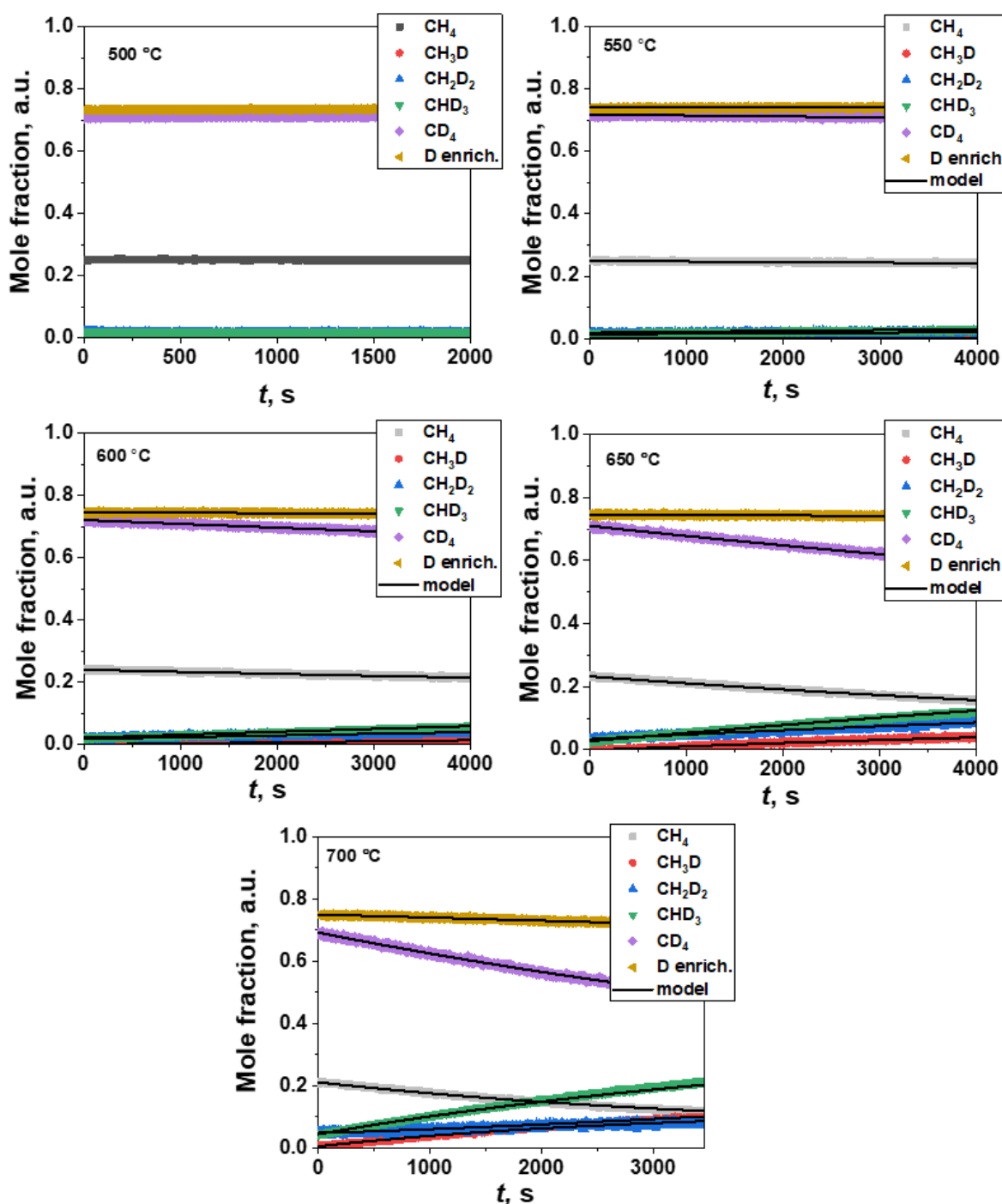


**Figure 1** Time dependencies of methane isotopologue fractions and  $\delta_M$  in methane obtained from the H/D exchange experiments at 100 Pa of  $\text{CH}_4$  (points) and fitted with the model of five exchange types (black lines).

The apparent activation energies for  $r$  and  $r_H$  were  $1.3 \pm 0.2$  and  $1.3 \pm 0.8$  eV. The values are comparable within the error margin and drastically higher than those in pure  $\text{H}_2$  atmosphere (0.28 and 0.24 eV, respectively) [38]. This indicates that both methane adsorption and hydrogen incorporation are determined by splitting C–H bonds of the species at the adsorption level of the oxide.

Figure 2b present power type dependencies of  $r$  on methane pressure at 550 °C. The figure shows that the methane partial reaction order in the pressure range of 100–500 Pa is equal to 1, suggesting that methane adsorption follows a monomolecular reaction mechanism.

To obtain detailed information on the elementary steps and intermediates involved in methane activation over LSGM, the probabilities of H/D exchange by the five exchange types ( $\chi_k$ ) and constraint parameters ( $c_1$ ,  $c_2$ , and  $c_3$ ) are proposed in [17, 53]. The values can be calculated using Equations (12)–(15). According to [53], if any of  $\chi_k$  is equal to 1, the mechanism of activation is one-step and determined by one of the respective types. If the sum of any two  $\chi_k$  is equal to 1, the mechanism is two-step, and in other cases the analysis of constraint parameters is required.

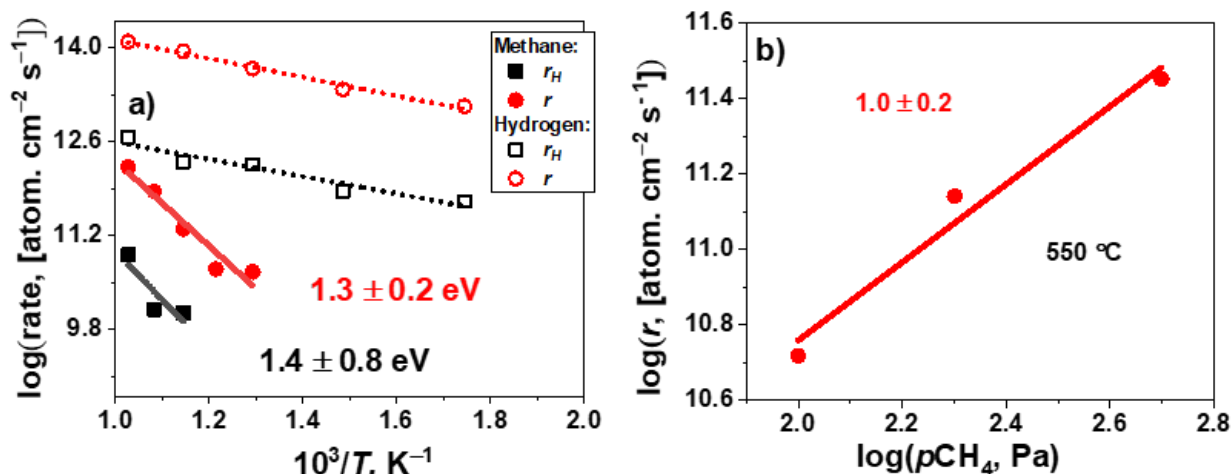


**Figure 2** Arrhenius plot of  $r$  and  $r_H$  obtained from H/D exchange between methane and LSGM at 100 Pa of CH<sub>4</sub> in comparison with  $r$  and  $r_H$  from H/D exchange between hydrogen and LSGM at 200 Pa of H<sub>2</sub> taken from [38] (a); Power type dependencies of  $r$  on pCH<sub>4</sub> obtained from H/D exchange between methane and LSGM at 550 °C in pCH<sub>4</sub> range of 100–500 Pa (b).

In general, if any constraint parameter is  $>1$ , the mechanism is presented by the distribution of parallel exchange steps; if it is  $<1$ , the kinetically non-equivalent adsorbed species with different hydrogen atomicities participate in some of the exchange steps. If all the parameters are 1, the mechanism comprises two-step dissociative adsorption and incorporation with single type of adsorbed species on the surface. A detailed discussion and mechanism analysis are presented in [53].

$$\chi_k = \frac{r_k}{r}, \quad (12)$$

$$c_1 = \frac{4}{\sqrt{6}} \frac{\sqrt{\chi_0 \chi_2}}{\chi_1}, \quad (13)$$

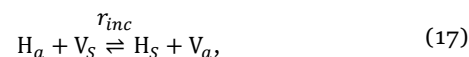
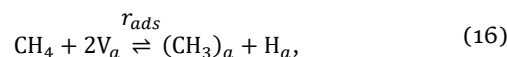
$$c_2 = \frac{3}{2} \frac{\sqrt{\chi_1 \chi_3}}{\chi_2}, \quad (14)$$

$$c_3 = \frac{4}{\sqrt{6}} \frac{\sqrt{\chi_4 \chi_2}}{\chi_3}. \quad (15)$$

Figure 3 presents the dependences of  $\chi_k$  on temperature, as calculated from fitting the model of the five exchange types to experimental data. The figure shows that the mechanism of methane activation for LSGM is temperature-dependent. At 550 °C, the kinetics of exchange is described by  $\chi_0 = 1$  which suggest [53] that the mechanism is one-step dissociative adsorption of  $r_0$  type. The mechanism is a simple indication of the absence of hydrogen participation from LSGM bulk in exchange.

In the temperature range of 600–650 °C, the mechanism is presented by a combination of non-zero  $\chi_0$  and  $\chi_1$  probabilities. According to [53], the combination of the types is associated with a two-step mechanism, which, in the case of LSGM, involves methane dissociative adsorption to methyl-adsorbed species and adsorbed hydrogen in the first step and the incorporation of the adsorbed hydrogen

to the solid in the second step. The mechanism can be described with equations (16) and (17):



where  $V_a$  is a formal, arbitrary vacant active site in the adsorption layer of LSGM,  $V_S$  is the active incorporation site of LSGM bulk,  $(\text{CH}_3)_a$  and  $\text{H}_a$  are adsorbed methyl species and hydrogen adsorbed atoms on the LSGM surface,  $\text{H}_S$  is incorporated hydrogen in LSGM bulk, and  $r_{ads}$  and  $r_{inc}$  are the rates of the respective steps. It should be noted that the notation  $V_a$  for the vacant adsorption sites on the LSGM surface is used in a formal manner to complete equation within the finite-surface interpretation of dissociative adsorption. In general, the adsorption sites for CH<sub>3</sub> and H are highly likely different. However, isotope exchange techniques do not provide direct information on the nature of the active sites, and additional techniques should be applied. A detailed discussion on this matter is presented in Section 4.4 below.

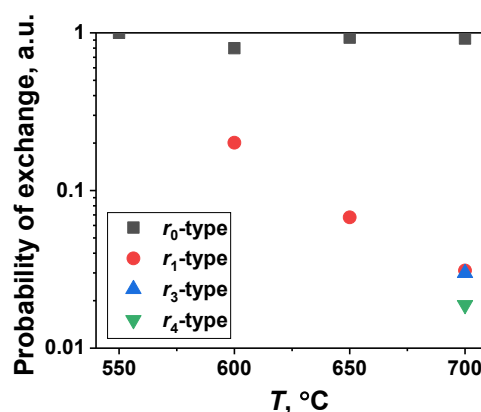
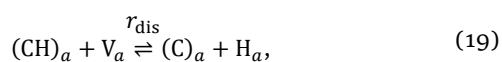
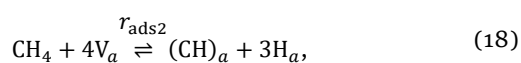


**Figure 3** Temperature dependencies of exchange probabilities  $\chi_0$ ,  $\chi_1$ ,  $\chi_3$ , and  $\chi_4$ .

The data at 700 °C are described by non-zero  $\chi_0$ ,  $\chi_1$ ,  $\chi_3$  and  $\chi_4$  probabilities, and, as a consequence, by the constraint parameters  $c_1 = 0$ ,  $c_2 = \infty$ , and  $c_3 = 0$ . According to [53], the values correspond to a mechanism with two independent parallel exchange pathways. In the case of LSGM, the first pathway is related to  $\chi_0$  and  $\chi_1$  probabilities, namely reactions (16) and (17). The second pathway is described by  $\chi_3$  and  $\chi_4$  probabilities. The analysis of exchange mechanisms presented in [53] shows that such a combination of these probabilities is related to a situation in which one of the four hydrogen atoms in the species in the adsorption layer of LSGM is kinetically different from the other three atoms. This indicates the existence of CH- species on the LSGM surface. Thus, this reaction pathway can be formally expressed by the following two additional reactions (18) and (19):



where  $(\text{CH})_a$  and  $(\text{C})_a$  are methyn and carbon adsorbed species in the adsorption layer of LSGM, and  $r_{\text{ads}2}$  and  $r_{\text{dis}}$  are the rates of the respective steps. Notably, reaction (18) is a formal representation of the first step in the exchange pathway. It is unlikely that three out of four C–H bonds were broken during the single exchange step. Rather, it indicates that during this pathway methane dissociation in a step-wise manner with the dissociative adsorption to  $(\text{CH}_3)_a$  and  $(\text{CH})_a$  to  $(\text{C})_a$  are the slow steps, whereas the dissociation of  $(\text{CH}_3)_a$  to  $(\text{CH}_2)_a$  and  $(\text{CH}_2)_a$  to  $(\text{CH})_a$  steps are significantly faster. The as-formed  $\text{H}_a$  at these steps can be incorporated into the oxide structure by step (17).

Summarizing the discussion of the mechanism, defining the rate-determining steps of exchange is necessary. Since the mechanism is one-step at 550 °C, this step is rate-determining in the whole exchange process. At temperatures higher than 550 °C,  $r_0$  types of exchange dominate, indicating that dissociative adsorption cannot be a rate-determining step. In the temperature range, considering that the mechanism includes two parallel pathways at 700 °C, the fastest pathway will be rate-determining, and Figure 3 shows that sum of  $\chi_0$  and  $\chi_1$  is higher than that of  $\chi_3$  and  $\chi_4$ . Therefore, steps (16) and (17) are rate-determining at 700 °C, and the limiting step of exchange in the temperature range 600–700 °C is hydrogen incorporation (17).

#### 4.2. Kinetics of H/D exchange between methane and hydrogen mixture and LSGM

Figure 4a-c presents time dependencies of D enrichment in methane ( $\delta_M$ ) and hydrogen ( $\delta_H = \frac{1}{2} \sum_{i=0}^2 ix_i$ ) obtained from the results of the H/D exchange experiments between the methane and hydrogen mixture with partial pressures of

100 and 200 Pa, respectively, and the LSGM in the temperature range 550–650 °C. The figure shows that increasing the temperature increases the exchange activity of LSGM for both methane and hydrogen in the mixture. The values of  $\delta_M$  decrease as time increases, whereas the values of  $\delta_H$  demonstrate the opposite trend. These results indicate that D atoms are transferred from methane to hydrogen during H/D exchange.

The model curves obtained from the fitting results of the data with the model of the three components are presented in Figure 4a-c with black lines. The curves closely match the experimental data, suggesting good agreement between the model and the obtained data.

Figure 4d presents the Arrhenius plot of the exchange rates ( $r_H$  and  $r_{H2}$ ) calculated from the fitting results and compared with the hydrogen surface exchange rates ( $r_H$ ) obtained in a pure methane atmosphere (see Section 4.1). According to the figure, among three possible exchange reactions in the three-component system (8)–(10), reaction (10), associated with surface exchange between  $\text{H}_2$  and LSGM, is not presented in the system of methane, hydrogen, and LSGM. Formally, this result contradicts the results of a previous study [38] that demonstrated the presence of surface exchange between pure  $\text{H}_2$  and LSGM. However, if we compare the rates of hydrogen surface exchange in pure  $\text{H}_2$  (see Figure 2a) with  $r_H$  and  $r_{H2}$  obtained in the mixture, the surface exchange between  $\text{H}_2$  and LSGM is much faster than the other process. Thus, considering the same initial isotope composition of LSGM and hydrogen, the hydrogen surface exchange between  $\text{H}_2$  and LSGM is too fast to be observed experimentally in the mixture of methane and hydrogen.

In contrast to the hydrogen surface exchange between  $\text{H}_2$  and LSGM, the heteromolecular exchange between  $\text{H}_2$  and  $\text{CH}_4$  and the surface exchange between  $\text{CH}_4$  and LSGM demonstrate measurable rates. The non-zero values of  $r_{H2}$  indicate the possibility of direct H/D exchange between methane and hydrogen in the LSGM adsorption layer. The appearance of this process suggests that as-formed hydrogen adsorbed atoms from methane and gaseous hydrogen are located at the same active sites (outermost oxygen atoms) [38, 39]. The apparent activation energy of the process is  $1.6 \pm 0.2$  eV and is close to the values for  $r_H$  and  $r$  in pure methane (Figure 2a). Thus, the limiting step of hydrogen migration between  $\text{H}_2$  and  $\text{CH}_4$  in the adsorption layer of LSGM is related to the formation or splitting C–H bonds in methane or methane-adsorbed species.

The comparison of  $r_H$  obtained in pure methane and in the mixture of methane and hydrogen shows that the values in the mixture exhibit the same temperature trend as the values in pure methane, but by 1.5 order of magnitude higher. This effect may be related to the higher concentration of protonic defects in LSGM bulk due to the increased incorporation of hydrogen from  $\text{H}_2$ .

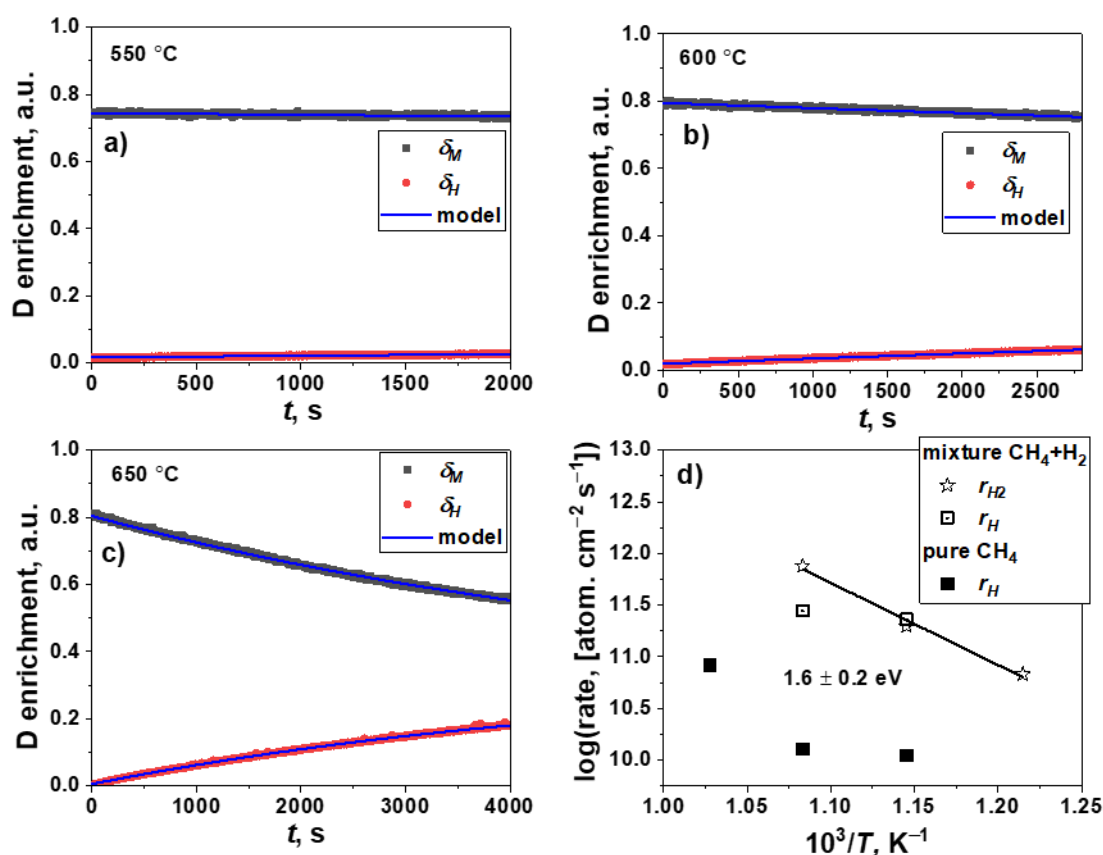


**Figure 4** Time dependencies of D enrichment in methane ( $\delta_M$ ) and hydrogen ( $\delta_H$ ) obtained from the results of H/D exchange in the mixture of methane (100 Pa) and hydrogen (200 Pa) over LSGM in the temperature range of 550–650 °C, where points are experimental data and lines are model curves (a–c); Arrhenius plot of hydrogen surface exchange ( $r_H$ ) and heteromolecular exchange ( $r_{H_2}$ ) calculated from the fitting results (d).

### 4.3. Carbon deposition

To estimate the stability of LSGM to the formation of carbon deposits on its surface during the H/D exchange process, the mean carbon fraction in the gas phase was evaluated ( $x_c = \frac{1}{5} \sum_{i=0}^4 x_i + \frac{1}{2} x_{CO} + \frac{1}{3} x_{CO_2}$ ). The increase in the value indicates the oxidation of methane, while the decrease indicates the formation of carbon deposits. Figure 5a presents the time dependences of  $x_c$  for all the temperatures under study. The figure shows the relatively constant values of  $x_c$  in the entire temperature range (500–700 °C), indicating that LSGM is relatively stable to the formation of carbon deposits at these temperatures.

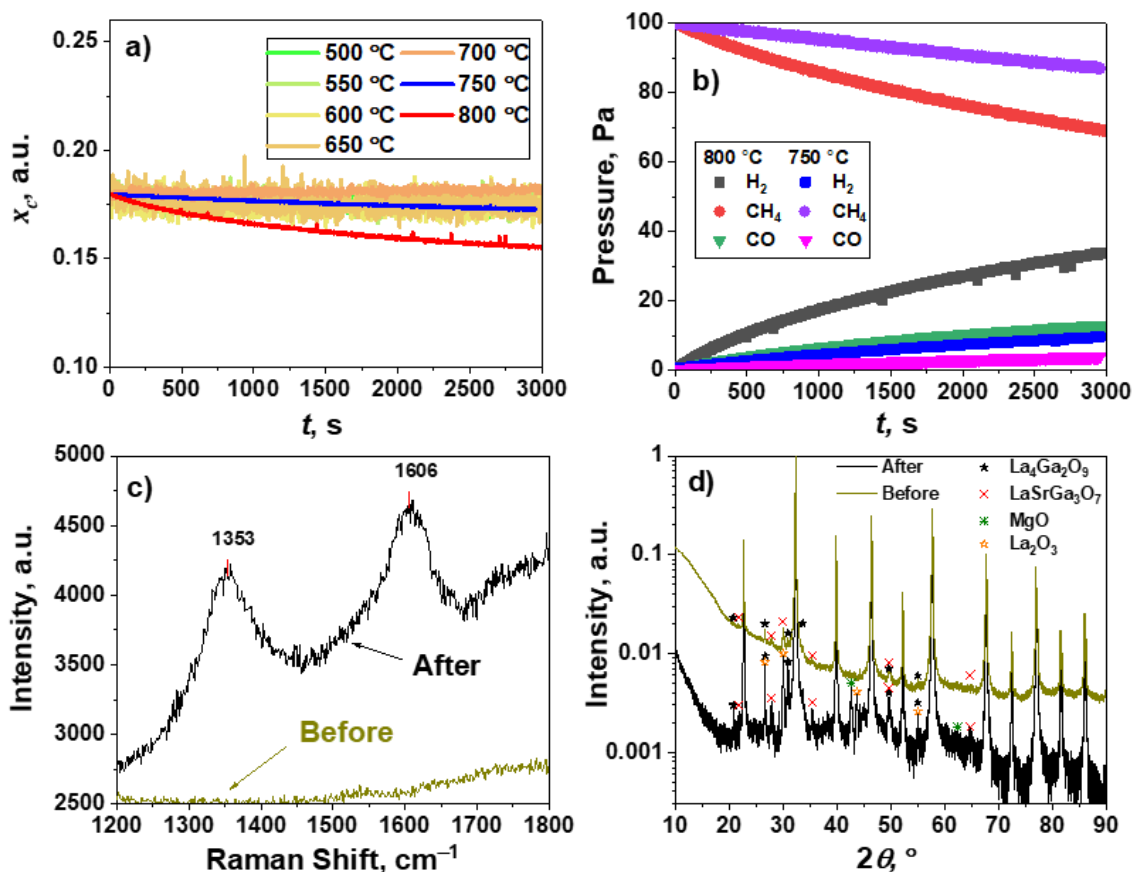
To estimate the temperature at which carbon deposition began, two additional annealing experiments of LSGM under 100 Pa of monoisotopic CH<sub>4</sub> were performed at temperatures of 750 °C and 800 °C. Figure 5a shows a slight decrease of  $x_c$  at these temperatures, demonstrating that carbon deposition starts at 750 °C. These results are in close agreement with those reported in [44], where the authors reported the formation of carbon deposits on the LSGM surface at 810 °C.

Figure 5b presents the time dependences of the partial pressures for the observed products of methane

decomposition at different temperatures. The figure demonstrates that methane is not only decomposed with the formation of H<sub>2</sub> but also oxidized to CO. The rates of these processes also increase with temperature. Since the experiments were conducted under dry and reductive conditions, the only source of O atoms for methane oxidation is LSGM.

To estimate the effect of carbon deposition and methane oxidation on LSGM, additional studies of LSGM with Raman spectroscopy and XRPD were performed. Figures 5c and 5d present the Raman spectra and XRPD profiles of LSGM before and after methane decomposition at 800 °C. Figure 5c shows the appearance of two broad peaks at 1353 and 1606 cm<sup>-1</sup>. The peaks typically associated with amorphous carbon [55] justify methane decomposition over the oxide surface.

The comparative plot of the XRPD profiles before and after experiments at 750–800 °C (Figure 5d) shows a selective increase in the intensity of the impurity peaks at 20.8, 26.6, 30, and 30.9° and the appearance of additional peaks at 42.6° and 43.7°. This behavior indicates the formation of additional phases, namely, La<sub>2</sub>O<sub>3</sub> and MgO, during the experiments. Thus, methane oxidation is related to the extraction of O atoms from LSGM, which results in LSGM decomposition.



**Figure 5** Time dependencies of the mean carbon fraction in the gas phase ( $x_c$ ) calculated from the results of H/D exchange experiments under 100 Pa of methane in the temperature range of 500–700 °C, and from annealing experiments under 100 Pa of methane in the temperature range 750–800 °C (a); time dependencies of  $CH_4$ ,  $H_2$ , and  $CO$  partial pressures obtained from annealing experiments under 100 Pa of methane in the temperature range 750–800 °C (b); Raman spectra of the LSGM before and after experiments at 800 °C (c); XRPD profiles of LSGM before and after annealing experiments at 800 °C (d).

#### 4.4. Mechanism of methane activation over LSGM

To summarize the presented study, it is necessary to discuss the complete methane activation mechanism. As presented in the Introduction, the mechanisms of methane oxidative coupling and partial oxidation considered in the literature are mainly based on the reaction schemes proposed for other systems. For the case of undoped  $LaGaO_3$  the most detailed schemes were discussed in [45, 46]. The schemes are summarized in Figures 6a and 6b. According to the figures, both reaction schemes demonstrate the splitting of methane conversion into two parallel pathways, namely, coupling and oxidation, with the main difference between the schemes being related to the role of oxygen in the reactions. According to [45], both conversion pathways are activated by  $LaGaO_3$  oxygen ( $O_s$ ) with different binding energies and adsorbed oxygen ( $O_{ads}$ ). Thus, the influence of molecular oxygen on the reaction is indirect, and the oxygen fills the vacancies ( $V_o$ ) in  $LaGaO_3$  structure refilling active sites of the catalyst. Conversely, the authors of [46] described the oxidation pathway by direct interaction of hydrocarbons with molecular oxygen in the catalyst's surface, while they related the oxidative coupling pathway with active oxygen atoms ( $O^+$ ).

The results presented in Sections 4.1–4.3 make it possible to clarify these schemes in terms of methane. Figure 6c

shows the kinetic scheme of methane activation over LSGM. The scheme demonstrates that the methane activation process is split into two parallel pathways, each of which is composed of reversible steps. The first step in both pathways is methane dissociative adsorption to the formation of methyl ( $CH_3$ )<sub>a</sub> species and hydrogen adsorbed atoms  $H_a$  that can either incorporate into the LSGM structure by interacting with protonic defects or recombine to form  $H_2$  molecules. In the second pathway, methyl species can reversibly and quickly dissociate to methyn species ( $CH$ )<sub>a</sub> and  $H_a$ , and methyn species can reversibly and slowly dissociate to  $H_a$  and adsorbed carbon atoms ( $C$ )<sub>a</sub>. The latter can irreversibly react with each other to form carbon deposits on the LSGM surface or be further irreversibly oxidized to form  $CO$ .

The comparison of methane activation scheme c) with schemes a) and b) demonstrates close agreement between the revealed activation mechanism and scheme a). Not only do both schemes include parallel methane reaction pathways but they also underline the contribution of structural oxygen atoms in methane oxidation. Additionally, scheme a) suggests that  $CO$  oxidation to  $CO_2$  is governed by adsorbed oxygen, which is in agreement with the obtained results: in dry reductive conditions, the LSGM surface lacks adsorbed oxygen, and oxidation proceeds only to  $CO$  species.

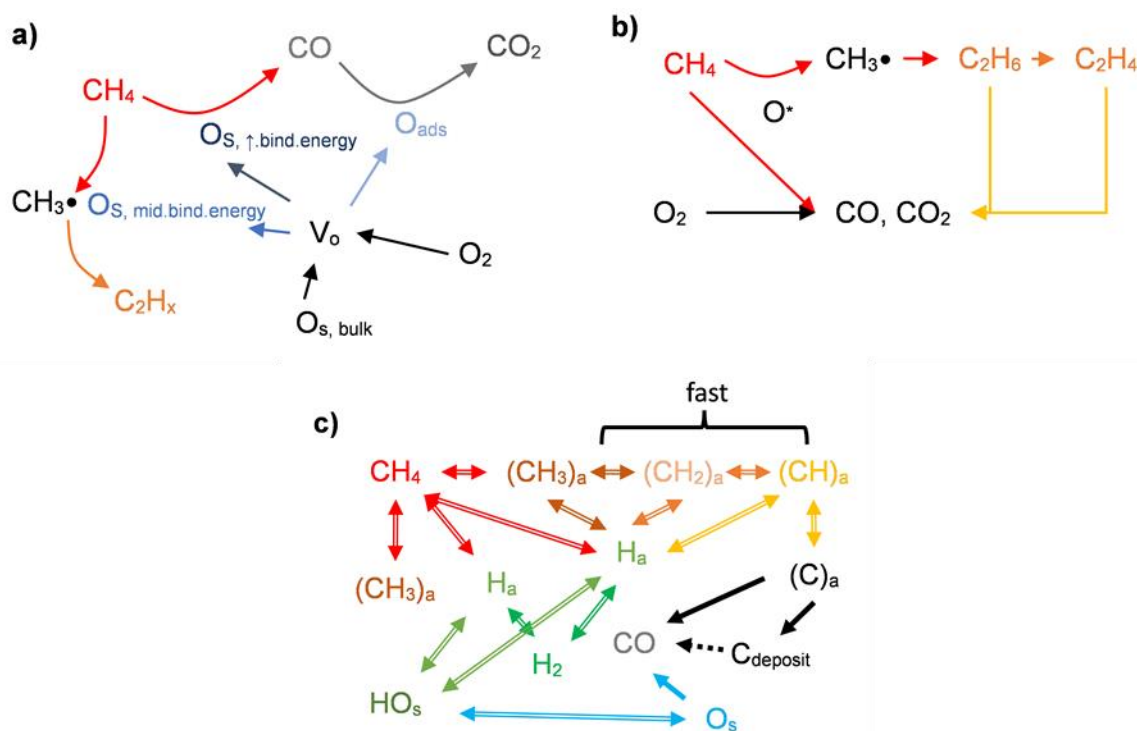


**Figure 6** Kinetic schemes of methane oxidative coupling and oxidation proposed for undoped  $\text{LaGaO}_3$  in papers [45] (a) and [46] (b); kinetic scheme of methane activation derived from H/D exchange and methane decomposition studies (see Sections 3.1–3.3) (c).

The nature of active sites ( $V_a$  in equations (16)–(19)) on LSGM for methane activation still requires additional studies. The authors of [45, 46] suggested that the sites are related to oxygen atoms. However, oxygen atoms are known to behave as active sites for  $\text{H}_2$  dissociative adsorption. If the same type of active sites is responsible for the reactions, competition should exist for the sites between methane and hydrogen. Such competition was observed in the case of Ni [56], where the increase in  $p_{\text{H}_2}$  decreases the hydrogen surface exchange rate for methane. In the case of LSGM, we see a completely different picture (Section 4.2): the addition of  $\text{H}_2$  promotes the hydrogen surface exchange rate for methane and creates an additional mass-transfer pathway related to the transfer of hydrogen between  $\text{H}_2$  and LSGM, suggesting that the active sites for methane and hydrogen adsorption are different.

Isotope exchange methods provide direct information only on the mass-transfer steps and atomicity of intermediates [53], which prevents direct clarification of the sites responsible for methane activation. However, in a recent study [17] on the LSGM-related perovskite system, namely,  $\text{La}_{1-x}\text{Sr}_x\text{ScO}_{3-\alpha}$  the authors analyzed the possible active sites on the oxide surface and found that  $\text{CH}_3$  species are preferably localized on the surface between La and Sc atoms, whereas the other  $\text{CH}_2$ ,  $\text{CH}$  and  $\text{C}$  species tend to occupy surface oxygen vacancies. The results agree with the mechanism often considered in the literature, which is related to the interaction of oxides and zeolites with methane [57–60], where the authors considered the binding of  $\text{CH}_3$  species to metal cations on the catalysts surface. The existence of two types of adsorption sites for methane species also explains the existence of the two-independent

pathways of methane adsorption and dissociation, and, as a consequence, the mechanism of carbon deposit formation. Nevertheless, additional studies are required on this matter.

To conclude this section, we can now discuss strategies to avoid carbon deposition on the LSGM surface, which can deactivate the catalyst's active sites within the revealed activation mechanism. As shown in Figure 6c, the resulting pathway for carbon deposit formation involves reversible stepwise methane dissociation to adsorbed carbon atoms that irreversibly form the deposition. The mechanism suggests two possible strategies to mitigate the process. The first involves the effect of sample composition. As discussed above, preceding studies on  $\text{La}_{1-x}\text{Sr}_x\text{ScO}_{3-\alpha}$  revealed oxygen vacancies in the outermost layers of the oxide as the active sites for carbon atom adsorption. Therefore, if the same sites are responsible for carbon adsorption over LSGM (which requires additional studies), a possible way to suppress carbon deposit formation on LSGM is to decrease the number of these sites, which can be achieved by varying the oxide composition. This approach, however, is likely to decrease the performance of LSGM in oxidative coupling reactions, which, as discussed in the Introduction, depends on oxygen bulk diffusivity.

The second strategy involves affecting the reaction steps responsible for carbon deposit formation through adjustments to operational conditions, namely temperature and gas-phase composition. The former is the simplest, as shown in Section 4.3, where the formation of amorphous carbon begins at temperatures  $>750^\circ\text{C}$ , while the catalytic activity of LSGM toward methane starts at  $550^\circ\text{C}$ . This indicates that carbon formation is a process with a high

activation barrier and can be managed by optimizing the working temperatures of the catalyst. The latter factor is associated with the reversibility of methane dissociation to adsorbed carbon ( $C_a$ ). The dissociation is accompanied by the formation of adsorbed hydrogen ( $H_a$ ), which means that if the number of  $H_a$  on the catalyst surface increases, the recombination of adsorbed methane species with  $H_a$  becomes more likely, effectively suppressing carbon deposition. This can be achieved by mixing methane with  $H_2$  or by using LSGM (or another proton-conducting material) as a membrane through which protons are supplied from another part of the membrane. The practical applicability of this strategy was demonstrated earlier in [52], where the authors studied a  $Ni-La_{0.9}Sr_{0.1}ScO_3$  catalyst in pure methane and a methane-hydrogen mixture, showing that carbon formation starts at 300 °C in pure methane, while it begins at 450 °C in the mixture. The disadvantage of this strategy is that the formation of  $CH_3$  species participating in oxidative coupling also produces  $H_a$ , which means that the strategy will inevitably decrease the performance of LSGM in oxidative coupling. Thus, accurate optimization of operational conditions is required to achieve both maximal performance and resistance of LSGM to carbon deposit formation.

## 5. Limitations

The major challenges in the investigation of methane activation mechanisms over solid catalysts using isotope exchange methods are the correct identification of the nature of active sites over the catalyst and the charge state of activation intermediates over the catalyst surface. Such challenges arise from the restrictions of the method. Isotope exchange is a kinetic method that is directly sensitive only to mass transfer reaction of labelled atoms.

To overcome these challenges, it is necessary to use combination of isotope exchange methods with other techniques, namely to determine the charge state of adsorbed species polarized isotope exchange can be used (combination of IE GPE method with electrochemical impedance spectroscopy), and to determine active sites of the catalysts combined IE GPE and in situ Raman / Infrared Spectroscopy or  $^1H$  NMR methods can be used.

## 6. Conclusions

For the first time, the mechanism of methane activation has been determined over the LSGM surface using H/D exchange with gas phase equilibration technique, Raman spectroscopy, and mass spectrometry gas phase analysis.

LSGM was found to exhibit catalytic activity to C–H bond splitting in methane in the temperature range 550–700 °C under  $CH_4$  pressures of 100, 200, and 500 Pa and  $H_2$  pressure of 200 Pa. At temperatures  $\geq 600$  °C, LSGM is capable of hydrogen surface exchange with methane, and hydrogen incorporation from methane to the oxide structure.

The mechanism of methane activation over LSGM was found to be composed of two parallel pathways, with the first pathway being methane dissociative adsorption to  $CH_3$  and H-adsorbed species formation, with H species being capable of incorporation into the LSGM structure to form protonic defects. The second pathway comprises methane dissociative adsorption to  $CH_3$  and H adsorbed species, fast stepwise dissociation of  $CH_3$  to  $CH_2$  and  $CH_2$  to CH, and slow dissociation of CH to C species, with the formation of H atoms at each dissociation step, which can then be incorporated into the oxide structure. The first pathway was found to be dominant across all studied temperature ranges, and the limiting step of activation was found to be H incorporation into the LSGM structure.

LSGM was stable in a methane atmosphere in the temperature range 550–700 °C. The increase in temperature to 750 °C and 800 °C leads to partial LSGM decomposition with the formation of  $La_2O_3$  and MgO phases, accompanied by the formation of carbon deposits and the methane oxidation to CO.

### Supplementary materials

No supplementary materials are available.

### Data availability statement

The data that support the findings of this study are available from the corresponding author upon reasonable request.

### Acknowledgments

The facilities of the Shared Access Center “Composition of Compounds” and the Unique Scientific Setup “Isotopic Exchange” of IHTE UB RAS were used. The author is grateful to E.G. Vovkotrub for Raman spectroscopy measurements and T.A. Kuznetsova for XRPD measurements.

### Author contributions

Conceptualization: D.M.Z.  
Data curation: D.M.Z.  
Formal Analysis: D.M.Z.  
Funding acquisition: D.M.Z.  
Investigation: D.M.Z.  
Methodology: D.M.Z.  
Project administration: D.M.Z.  
Resources: D.M.Z.  
Software: D.M.Z.  
Supervision: D.M.Z.  
Validation: D.M.Z.  
Visualization: D.M.Z.  
Writing – original draft: D.M.Z.  
Writing – review & editing: D.M.Z.

### Conflict of interest

The author declares no conflict of interest

### Additional information

Author ID:  
Dmitriy M. Zakharov, Scopus ID [57195552751](https://orcid.org/57195552751);  
Website:  
Institute of High Temperature Electrochemistry UB RAS,  
[https://ihite.ru/?page\\_id=3106](https://ihite.ru/?page_id=3106).

## References

- Sadykov VA, Ereemeev NF, Sadovskaya EM, Shlyakhtina AV, Pikalova EY, Osinkin DA, Yaremchenko AA. Design of materials for solid oxide fuel cells, permselective membranes, and catalysts for biofuel transformation into syngas and hydrogen based on fundamental studies of their real structure, transport properties, and surface reactivity. *Curr Opin Green Sustain Chem.* 2022;33:100558. doi:[10.1016/j.cogsc.2021.100558](https://doi.org/10.1016/j.cogsc.2021.100558)
- Duan CC, Tong JH, Shang M, Nikodemski S, Sanders M, Ricote S, Almansoori A, O'Hayre R. Readily processed protonic ceramic fuel cells with high performance at low temperatures. *Sci.* 2015;349:1321–1326. doi:[10.1126/science.aab3987](https://doi.org/10.1126/science.aab3987)
- Shi N, Xue S, Xie Y, Yang Y, Huan D, Pan Y, Peng R, Xia C, Zhan Z, Lu Y. Co-generation of electricity and olefin via proton conducting fuel cells using  $(\text{Pr}_{0.3}\text{Sr}_{0.7})_{0.9}\text{Ni}_{0.1}\text{Ti}_{0.9}\text{O}_3$  catalyst layers. *Appl Catal B Environ.* 2020;272:118973. doi:[10.1016/j.apcatb.2020.118973](https://doi.org/10.1016/j.apcatb.2020.118973)
- Vollestad E, Strandbakke R, Tarach M, Catalán-Martínez D, Fontaine M-L, Beeaff D, Clark DR, Serra JM, Norby T. Mixed proton and electron conducting double perovskite anodes for stable and efficient tubular proton ceramic electrolyzers. *Nat Mater.* 2019;18:752–759. doi:[10.1038/s41563-019-0388-2](https://doi.org/10.1038/s41563-019-0388-2)
- Bausá N, Escolástico S, Serra JM. Direct  $\text{CO}_2$  conversion to syngas in a  $\text{BaCe}_{0.2}\text{Zr}_{0.7}\text{Y}_{0.1}\text{O}_{3-\delta}$ -based proton-conducting electrolysis cell. *J  $\text{CO}_2$  Util.* 2019;34:231–238. doi:[10.1016/j.jcou.2019.05.037](https://doi.org/10.1016/j.jcou.2019.05.037)
- Tucker MC. Progress in metal-supported solid oxide electrolysis cells: A review. *Int J Hydrogen Energ.* 2020;45:24203–24218. doi:[10.1016/j.ijhydene.2020.06.300](https://doi.org/10.1016/j.ijhydene.2020.06.300)
- Duan C, Kee R, Zhu H, Sullivan N, Zhu L, Bian L, Dylan J, O'Hayre R. Highly efficient reversible protonic ceramic electrochemical cells for power generation and fuel production. *Nat Energy.* 2019;4:230–240. doi:[10.1038/s41560-019-0333-2](https://doi.org/10.1038/s41560-019-0333-2)
- Langguth J, Dittmeyer R, Hofmann H, Tomandl G. Studies on oxidative coupling of methane using high-temperature proton-conducting membranes. *Appl Catal A Gen.* 1997;158:287–305. doi:[10.1016/S0926-860X\(96\)00375-4](https://doi.org/10.1016/S0926-860X(96)00375-4)
- Karagiannakis G, Zisekas S, Kokkofitis C, Stoukides M. Effect of  $\text{H}_2\text{O}$  presence on the propane decomposition reaction over Pd in a proton conducting membrane reactor. *Appl Catal A Gen.* 2006;301:265–271. doi:[10.1016/j.apcata.2005.12.017](https://doi.org/10.1016/j.apcata.2005.12.017)
- Malerød-Fjeld H, Clark D, Yuste-Tirados I, Zanón R, Catalán-Martínez D, Beeaff D, Morejudo SH, Vestre PK, Norby T, Haugsrud R, Serra JM, Kjølsseth C. Thermo-electrochemical production of compressed hydrogen from methane with near-zero energy loss. *Nat Energy.* 2019;2:923–931. doi:[10.1038/s41560-017-0029-4](https://doi.org/10.1038/s41560-017-0029-4)
- Morejudo SH, Zanón R, Escolástico S, Yuste-Tirados I, Malerød-Fjeld H, Vestre PK, Coors WG, Martínez A, Norby T, Serra JM, Kjølsseth C. Direct conversion of methane to aromatics in a catalytic co-ionic membrane reactor. *Sci.* 2016;353:563–6. doi:[10.1126/science.aag0274](https://doi.org/10.1126/science.aag0274)
- Meng Y, Gao J, Zhao Z, Amoroso J, Tong J, Brinkman KS. Review: recent progress in low-temperature proton-conducting ceramics. *J Mater Sci.* 2019;54:9291–9312. doi:[10.1007/s10853-019-03559-9](https://doi.org/10.1007/s10853-019-03559-9)
- Merkle R, Hoedl MF, Raimondi G, Zohourian R, Maier J. Oxides with Mixed Protonic and Electronic Conductivity. *Annu Rev Mater Res.* 2021;51:461–493. doi:[10.1146/annurev-matsci-091819-010219](https://doi.org/10.1146/annurev-matsci-091819-010219)
- Osinkin D, Porotnikova N, Khodimchuk AV. Features of exchange kinetics of  $\text{BaFeO}_{3-\delta}$ -based triple-conducting materials: current state of research. *J Mater Chem A.* 2025;13:27907. doi:[10.1039/D5TA03192C](https://doi.org/10.1039/D5TA03192C)
- Danilov NA, Starostina IA, Starostin GN, Kasyanova AV, Medvedev DA, Shao Z. Fundamental Understanding and Applications of Protonic Y- and Yb-Coped  $\text{Ba}(\text{Ce},\text{Zr})\text{O}_3$  Perovskites: State-of-the-Art and Perspectives. *Adv Energy Mater.* 2023;13:2302172. doi:[10.1002/aenm.202302175](https://doi.org/10.1002/aenm.202302175)
- Egorova A, Belova K, Animitsa I. Doping effects on the structure, transport properties, and chemical stability of  $\text{LaInO}_3$  perovskite: A review. *Chim Techno Acta.* 2025;12(1):1211. doi:[10.15826/chimtech.2025.12.1.11](https://doi.org/10.15826/chimtech.2025.12.1.11)
- Zakharov DM, Zhuravlev NA, Denisova TA, Belozherov AS, Stroeva AYU, Vovkotrub EG, Farlenkov AS, Ananyev MV. Catalytic methane activation over  $\text{La}_{1-x}\text{Sr}_x\text{ScO}_{3-\alpha}$  proton-conducting oxide surface: a comprehensive study. *J Catal.* 2021;394:67–82. doi:[10.1016/j.jcat.2020.12.011](https://doi.org/10.1016/j.jcat.2020.12.011)
- Kreuer KD. Proton-conducting oxides. *Annu Rev Mater Res.* 2003;33:333–359. doi:[10.1146/annurev.matsci.33.022802.091825](https://doi.org/10.1146/annurev.matsci.33.022802.091825)
- Ananyev MV, Farlenkov AS, Kurumchin EKh. Isotopic exchange between hydrogen from the gas phase and proton-conducting oxides: Theory and experiment. *Int J Hydrogen Energy.* 2018;43:13373–13382. doi:[10.1016/j.ijhydene.2018.05.150](https://doi.org/10.1016/j.ijhydene.2018.05.150)
- Gordeev E, Porotnikova N. Approaches for the preparation of dense ceramics and sintering aids for Sr/Mg doped lanthanum gallate: focus review. *Electrochem Mater Technol.* 2023;2:20232022. doi:[10.15826/elmattech.2023.2.022](https://doi.org/10.15826/elmattech.2023.2.022)
- Gordeev E, Belyakov S, Antonova E, Osinkin D. Highly Conductive Fe-Doped  $(\text{La},\text{Sr})(\text{Ga},\text{Mg})\text{O}_{3-\delta}$  Solid-State Membranes for Electrochemical Application. *Membranes.* 2023;13(5):502. doi:[10.3390/membranes13050502](https://doi.org/10.3390/membranes13050502)
- Huang K, Tichy RS, Goodenough JB. Superior Perovskite Oxide-Ion Conductor; Strontium- and Magnesium-Doped  $\text{LaGaO}_3$ : I, Phase Relationships and Electrical Properties. *J Am Ceram Soc.* 2005;81:2565–2575. doi:[10.1111/j.1151-2916.1998.tb02662.x](https://doi.org/10.1111/j.1151-2916.1998.tb02662.x)
- Kharton VV, Shaula AL, Vyshatko NP, Marques FMB. Electron-hole transport in  $(\text{La}_{0.9}\text{Sr}_{0.1})_{0.98}\text{Ga}_{0.8}\text{Mg}_{0.2}\text{O}_{3-\delta}$  electrolyte: effects of ceramic microstructure. *Electrochimica Acta.* 2003;48:1817–1828. doi:[10.1016/S0013-4686\(03\)00247-0](https://doi.org/10.1016/S0013-4686(03)00247-0)
- Li M, Zhang Y, An M, Lu Z, Huang X, Xiao J, Wei B, Zhu X, Su W. Synthesis and characterization of  $\text{La}_{0.9}\text{Sr}_{0.1}\text{Ga}_{0.8}\text{Mg}_{0.2}\text{O}_{3-\delta}$  intermediate-temperature electrolyte using conventional solid-state reaction. *J Power Sources.* 2012;218:233–236. doi:[10.1016/j.jpowsour.2012.06.101](https://doi.org/10.1016/j.jpowsour.2012.06.101)
- Huang K, Feng M, Goodenough JB. Sol-Gel Synthesis of a New Oxide-Ion Conductor Sr- and Mg-Doped  $\text{LaGaO}_3$  Perovskite. *J Am Ceram Soc.* 1996;79:1100–1104. doi:[10.1111/j.1151-2916.1996.tb08554.x](https://doi.org/10.1111/j.1151-2916.1996.tb08554.x)
- Morales M, Roa JJ, Tartaj J, Segarra M. A review of doped lanthanum gallates as electrolytes for intermediate temperature solid oxides fuel cells: From materials processing to electrical and thermo-mechanical properties. *J Eur Ceram Soc.* 2016;36:1–16. doi:[10.1016/j.jeurceramsoc.2015.09.025](https://doi.org/10.1016/j.jeurceramsoc.2015.09.025)
- Hayashi H, Suzuki M, Inaba H. Thermal expansion of Sr- and Mg-doped  $\text{LaGaO}_3$ . *Solid State Ionics.* 2000;128:131–139. doi:[10.1016/S0167-2738\(99\)00346-X](https://doi.org/10.1016/S0167-2738(99)00346-X)
- He C, Wu J, Lee Y. Correlation between conductivity and structural parameters in Sr-doped  $\text{LaMO}_3$  (M = Al, Ga, In, Er, and Y) for solid oxide membranes. *Solid State Ionics.* 2023;399:116315. doi:[10.1016/j.ssi.2023.116315](https://doi.org/10.1016/j.ssi.2023.116315)
- Ishihara T. Oxygen surface exchange and diffusion in  $\text{LaGaO}_3$  based perovskite type oxides. *Solid State Ionics.* 1998;113–115:593–600. doi:[10.1016/S0167-2738\(98\)00390-7](https://doi.org/10.1016/S0167-2738(98)00390-7)
- Yamaji K, Horita T, Sakai N, Yokokawa H. Comparison between  $\text{La}_{0.9}\text{Ba}_{0.1}\text{Ga}_{0.8}\text{Mg}_{0.2}\text{O}_{2.85}$  and  $\text{La}_{0.9}\text{Sr}_{0.1}\text{Ga}_{0.8}\text{Mg}_{0.2}\text{O}_{2.85}$  as SOFCs electrolytes. *Solid State Ionics.* 2002;152–153:517–523. doi:[10.1016/S0167-2738\(02\)00352-1](https://doi.org/10.1016/S0167-2738(02)00352-1)
- Vdovin GK, Kurumchin EKh, Isaeva EV, Bronin DI. Isotopic Exchange and Oxygen Diffusion in the  $\text{La}_{0.88}\text{Sr}_{0.12}\text{Ga}_{0.82}\text{Mg}_{0.18}\text{O}_{3-\alpha}$ -Molecular Oxygen System. *Russ J Electrochem.* 2001;37:304–307. doi:[10.1023/A:1009085532471](https://doi.org/10.1023/A:1009085532471)
- Kurumchin EKh, Ananjev MV, Vdovin GK, Surkova MG. Exchange kinetics and diffusion of oxygen in systems based on lanthanum gallate. *Russ J Electrochem.* 2010;46:205–211. doi:[10.1134/S1023193510020126](https://doi.org/10.1134/S1023193510020126)

33. Porotnikova N, Khodimchuk A, Gordeev E, Osinkin D. Effect of doping with iron and cations deficiency in the high conductive electrolyte  $\text{La}_{0.8}\text{Sr}_{0.2}\text{Ga}_{0.8}\text{Mg}_{0.2}\text{O}_{3-\delta}$  on oxygen exchange kinetics. *Solid State Ionics*. 2024;417:116704. doi:[10.1016/j.ssi.2024.116704](https://doi.org/10.1016/j.ssi.2024.116704)
34. Filonova E, Medvedev D. Recent Progress in the Design, Characterisation and Application of  $\text{LaAlO}_3$ - and  $\text{LaGaO}_3$ -Based Solid Oxide Fuel Cell Electrolytes. *Nanomater*. 2022;12:1991. doi:[10.3390/nano12121991](https://doi.org/10.3390/nano12121991)
35. Ma G, Zhang F, Zhu J, Meng G. Proton Conduction in  $\text{La}_{0.9}\text{Sr}_{0.1}\text{Ga}_{0.8}\text{Mg}_{0.2}\text{O}_{3-\alpha}$ . *Chem Mater*. 2006;18:6006-6011. doi:[10.1021/cm0612954](https://doi.org/10.1021/cm0612954)
36. Zhang F, Yang Q, Pan B, Xu R, Wang H, Ma G. Proton conduction in  $\text{La}_{0.9}\text{Sr}_{0.1}\text{Ga}_{0.8}\text{Mg}_{0.2}\text{O}_{3-\alpha}$  ceramic prepared via micro-emulsion method and its application in ammonia synthesis at atmospheric pressure. *Mater Lett*. 2007;61:4144-4148. doi:[10.1016/j.matlet.2007.01.060](https://doi.org/10.1016/j.matlet.2007.01.060)
37. Chen C, Ma G. Preparation, proton conduction, and application in ammonia synthesis at atmospheric pressure of  $\text{La}_{0.9}\text{Ba}_{0.1}\text{Ga}_{1-x}\text{Mg}_x\text{O}_{3-\alpha}$ . *J Mater Sci*. 2008;43:5109-5114. doi:[10.1007/s10853-008-2747-2](https://doi.org/10.1007/s10853-008-2747-2)
38. Zakharov DM, Gordeev EV, Fedorova KA. Hydrogen activation and surface exchange over  $\text{La}_{0.8}\text{Sr}_{0.2}\text{Ga}_{0.8}\text{Mg}_{0.2}\text{O}_{3-z}$ . *J Solid State Chem*. 2025;341:125073. doi:[10.1016/j.jssc.2024.125073](https://doi.org/10.1016/j.jssc.2024.125073)
39. Zakharov DM, Gordeev EV, Shadrina MA, Suntsov AYU, Osinkin DA. Effect of Fe-doping and red-ox conditions on hydrogen surface exchange between  $\text{H}_2$  and lanthanum gallate. *Appl Surf Sci*. 2025;714:164383. doi:[10.1016/j.apsusc.2025.164383](https://doi.org/10.1016/j.apsusc.2025.164383)
40. Ishihara T, Hiei Y, Takita Y. Oxidative reforming of methane using solid oxide fuel cell with  $\text{LaGaO}_3$ -based electrolyte. *Solid State Ionics*. 1995;79:371-375. doi:[10.1016/0167-2738\(95\)00090-s](https://doi.org/10.1016/0167-2738(95)00090-s)
41. Ishihara T, Takita Y. Partial oxidation of methane into syngas with oxygen permeating ceramic membrane reactors. *Catal Surv Jpn*. 2001;4:125-133. doi:[10.1023/A:1011407421210](https://doi.org/10.1023/A:1011407421210)
42. Ishihara T, Tsuruta Y, Todaka T, Nishiguchi H, Takita Y. Fe doped  $\text{LaGaO}_3$  perovskite oxide as an oxygen separating membrane for  $\text{CH}_4$  partial oxidation. *Solid State Ionics*. 2002;152-153:709-714. doi:[10.1016/s0167-2738\(02\)00413-7](https://doi.org/10.1016/s0167-2738(02)00413-7)
43. Bi Z, Matsumoto H, Ishihara T. Solid-state amperometric  $\text{CH}_4$  sensor using,  $\text{LaGaO}_3$ -based electrolyte. *Solid State Ionics*. 2008;179:1641-1644. doi:[10.1016/j.ssi.2007.11.018](https://doi.org/10.1016/j.ssi.2007.11.018)
44. Omoze Igenegbai V, Almallahi R, Meyer RJ, Linic S. Oxidative Coupling of Methane over Hybrid Membrane/Catalyst Active Centers: Chemical Requirements for Prolonged Lifetime. *ACS Energy Lett*. 2019;4:1465-1470. doi:[10.1021/acsenergylett.9b01075](https://doi.org/10.1021/acsenergylett.9b01075)
45. Sim Y, Kwon D, An S, Ha J-M, Oh T-S, Jung JC. Catalytic behavior of  $\text{ABO}_3$  perovskites in the oxidative coupling of methane. *Mol Catal*. 2020;489:110925. doi:[10.1016/j.mcat.2020.110925](https://doi.org/10.1016/j.mcat.2020.110925)
46. Gan R, Nishida Y, Haneda M. Effect of B Site Substitution on the Catalytic Activity of La-Based Perovskite for Oxidative Coupling of Methane. *Phys Status Solidi B*. 2022;259:2100544. doi:[10.1002/pssb.202100544](https://doi.org/10.1002/pssb.202100544)
47. Yamashita H, Machiba Y, Tomita A. Oxidative coupling of methane with peroxide ions over barium-lanthanum-oxygen mixed oxide. *Appl Catal A Gen*. 1991;79:203-214. doi:[10.1016/0926-860X\(91\)80006-K](https://doi.org/10.1016/0926-860X(91)80006-K)
48. Takanabe K. Catalytic Conversion of Methane: Carbon Dioxide Reforming and Oxidative Coupling. *J Jpn Pet Inst*. 2012;55:1-12. English. Available from: [https://www.jst.go.jp/article/jpi/55/1/55\\_1\\_1\\_pdf](https://www.jst.go.jp/article/jpi/55/1/55_1_1_pdf), Accessed on 14 October 2025
49. Wang H, Cong Y, Yang W. Oxidative coupling of methane in  $\text{Ba}_{0.5}\text{Sr}_{0.5}\text{Co}_{0.8}\text{Fe}_{0.2}\text{O}_{3-\delta}$  tubular membrane reactors. *Catal Today*. 2005;104:160-167. doi:[10.1016/j.cattod.2005.03.079](https://doi.org/10.1016/j.cattod.2005.03.079)
50. Luo L, Tang X, Wang W, Wang Y, Sun S, Qi F, Huang W. Methyl Radicals in Oxidative Coupling of Methane Directly Confirmed by Synchrotron VUV Photoionization Mass Spectroscopy. *Sci Rep*. 2013;3:1625. doi:[10.1038/srep01625](https://doi.org/10.1038/srep01625)
51. Ananyev MV, Zakharov DM. H/D isotopic exchange between methane and a proton-conducting oxide: theory and experiment. *Catal Sci Technol*. 2020;10:3561. doi:[10.1039/c9cy02566a](https://doi.org/10.1039/c9cy02566a)
52. Zakharov DM, Ananyev MV. Methane dissociation mechanism on Ni-La<sub>1-x</sub>Sr<sub>x</sub>ScO<sub>3-δ</sub> cermet for proton ceramic electrochemical devices. *Int J Hydrogen Energy*. 2022;47:16824-16839. doi:[10.1016/j.ijhydene.2022.03.171](https://doi.org/10.1016/j.ijhydene.2022.03.171)
53. Zakharov DM, Ananyev MV. Interaction of hydrocarbons containing four hydrogen atoms with condensed phases: Classification of H/D exchange mechanisms and mechanism selection algorithm. *J Catal*. 2025;448:116173. doi:[10.1016/j.jcat.2025.116173](https://doi.org/10.1016/j.jcat.2025.116173)
54. Gucci L, Hoffer T, Tetenyl P, Shestov AA. Kinetic and tracer studies on methanol conversion over supported platinum catalysts. *Chem Eng Commun*. 1989;83:75-86. doi:[10.1080/00986448908940653](https://doi.org/10.1080/00986448908940653)
55. Dychalska A, Popielarski P, Franków W, Fabisiak K, Paprocki K, Szybowicz M. Study of CVD diamond layers with amorphous carbon admixture by Raman scattering spectroscopy. *Mater Sci Pol*. 2015;33:799-805. doi:[10.1515/msp-2015-0067](https://doi.org/10.1515/msp-2015-0067)
56. Kemball C. Reaction of methane and deuterium on evaporated nickel catalysts. *Proc R Soc Lond A*. 1951;207(1091):539-554. doi:[10.1098/rspa.1951.0139](https://doi.org/10.1098/rspa.1951.0139)
57. Larson JG, Hall WK. VII. Studies of hydrogen held by solids. The exchange of the hydroxyl group of alumina and silica-alumina catalyst with deuterated methane. *J Phys Chem-US*. 1985;69:3080-3089. doi:[10.1021/j100893a044](https://doi.org/10.1021/j100893a044)
58. Quanzhi L, Amenomiya Y. Exchange reaction of methane on some oxide catalyst. *Appl Catal*. 1986;23(1):173-182. doi:[10.1016/S0166-9834\(00\)81460-8](https://doi.org/10.1016/S0166-9834(00)81460-8)
59. Vaylon J, Engelhardt J, Kallo D, Hegedus M. The activation of  $\text{CD}_4$  for H/D exchange over H-zeolites. *Catal Lett*. 2002;82(1-2):29-35. doi:[10.1023/A:1020579705752](https://doi.org/10.1023/A:1020579705752)
60. Engelhardt J, Vaylon J. H/D exchange between  $\text{CD}_4$  and the OH-groups of H-zeolites and  $\gamma\text{-Al}_2\text{O}_3$ . *React Kinet Catal Lett*. 2001;74:217-224. doi:[10.1023/A:1017972624428](https://doi.org/10.1023/A:1017972624428)